Dalton Transactions

ROYAL SOCIETY OF CHEMISTRY

PAPER

Cite this: *Dalton Trans.*, 2020, **49**, 12401

A trimeric tri-Tb^{3+} including antimonotungstate and its Eu^{3+}/Tb^{3+}/Dy^{3+}/Gd^{3+}-codoped species with luminescence properties†

Xin Xu,[a] Changtong Lu,[a,b] Saisai Xie,[a] Lijuan Chen*[a] and Junwei Zhao *[a]

A trimeric tri-Tb^{3+}-including antimonotungstate (AMT) hybrid $Na_{17}\{(WO_4)[Tb(H_2O)(Ac)(B\text{-}\alpha\text{-}SbW_9O_{31}(OH)_2)]_3\}\cdot 50H_2O$ (**Tb_3W_{28}**) was successfully synthesized, in which the capped tetrahedral $\{WO_4\}$ group plays a significant template role in directing the aggregation of three $[B\text{-}\alpha\text{-}SbW_9O_{33}]^{9-}$ fragments and three Tb^{3+} ions. Eu^{3+}/Tb^{3+}/Dy^{3+}/Gd^{3+}-codoped AMT materials based on **Tb_3W_{28}** were firstly prepared and their luminescence properties were investigated. The red emitter Eu^{3+}, yellow emitter Dy^{3+}, and nonluminous Gd^{3+} ions were codoped into **Tb_3W_{28}** to substitute Tb^{3+} ions for investigating the energy transfer (ET) mechanism among Eu^{3+}, Tb^{3+}, and Dy^{3+} ions. Upon the $^6H_{15/2} \rightarrow {}^4I_{13/2}$ excitation at 389 nm of the Dy^{3+} ion, the ET_1 mechanism ($Dy^{3+} \rightarrow Tb^{3+}$) was confirmed as a non-radiative dipole–dipole interaction. Under the $^7F_6 \rightarrow {}^5L_{10}$ excitation at 370 nm of the Tb^{3+} ion, the ET_2 mechanism ($Tb^{3+} \rightarrow Eu^{3+}$) was identified as a non-radiative quadrupole–quadrupole interaction. Under excitation at 389 nm, the two-step successive $Dy^{3+} \rightarrow Tb^{3+} \rightarrow Eu^{3+}$ ET_3 process was proved in **$Dy_{1.2}Tb_{3z}Eu_{0.03}Gd_{1.77-3z}W_{28}$**. Through changing the excitation wavelengths, the emission color of **$Dy_{1.2}Tb_{1.2}Eu_{0.03}Gd_{0.57}W_{28}$** can vary from blue to yellow, in which a near-white-light emission case was observed upon excitation at 378 nm. This work not only provides a systematic ET mechanism study of hetero-Ln-codoped AMTs, but also offers some useful guidance for designing novel performance-oriented Ln-codoped polyoxometalate-based materials.

Received 3rd June 2020,
Accepted 7th August 2020

DOI: 10.1039/d0dt01985b

rsc.li/dalton

Introduction

In the past few decades, polyoxometalates (POMs), a famous family of anionic high-oxidation-state early transition-metal (TM) clusters, have made considerable progress on the intricate ingredients, intriguing structures, and potential applications in electrochemical biosensors, energy, luminescence, catalysis and proton conductivity, *etc*.[1–10] In POM assembly, it is imperative to realize structure design by the prediction, rationality, and controllability of experimental conditions.[11,12] For instance, the strong Lewis acidity of the vacant sites of polyoxotungstate (POT) fragments makes them exhibit strong affinity toward TM or lanthanide (Ln) ions.[13–16] Many experiments have revealed that carboxylic organic ligands can regulate and control the competitive reactions between different metal ions, and link various POT fragments together to construct oligomeric, polymeric, or extended structures.[17–19] Some effective preparative strategies such as the building block method, the template-directing assembly, and the bottom-up concept have been developed recently.[20–22] However, designing and synthesizing novel poly(POT) clusters with anticipative compositions, shapes, sizes, and dimensions still have a long way to go.

In the past few years, the great developments of Ln-containing POTs (LnCPOTs) have been exemplified because trivalent Ln ions possess large ionic radii, high coordination numbers, and flexible coordination modes, which are conducive to the construction of LnCPOT aggregates.[23–25] Among LnCPOTs, some Ln-containing antimonotungstates (LnCAMTs) based on $[B\text{-}\alpha\text{-}SbW_9O_{33}]^{9-}$ fragments have been reported, even including some organic–inorganic hybrid LnCAMTs (OIHLnCAMTs).[26,27] For example, in 2002, Gouzerh's group reported a tri-Ce^{3+}-containing tetrameric AMT $[(B\text{-}\alpha\text{-}SbW_9O_{33})_4\{WO_2(H_2O)\}_2Ce_3(H_2O)_8(Sb_4O_4)]^{19-}$ with an $\{Sb_4O_4\}$ cluster (Fig. 1a).[28] In 2011, Kortz *et al.* prepared a group of sandwich-type di-Ln-substituted AMTs $[Ln_2(H_2O)_8Sb_2W_{20}O_{70}]^{8-}$ (Ln = Yb^{3+}, Lu^{3+}, Y^{3+}), forming a 1-D chain structure through Ln linkers (Fig. 1b).[29] In 2014, Zhao and co-workers reported a series of threonine-

[a]*Henan Key Laboratory of Polyoxometalate Chemistry, College of Chemistry and Chemical Engineering, Henan University, Kaifeng, Henan 475004, China. E-mail: ljchen@henu.edu.cn, zhaojunwei@henu.edu.cn*
[b]*China Tobacco Henan Industrial Company Ltd., Zhengzhou, Henan 475000, China*

†Electronic supplementary information (ESI) available: The refinement details and additional figures. CCDC 2007609. For ESI and crystallographic data in CIF or other electronic format see DOI: 10.1039/D0DT01985B

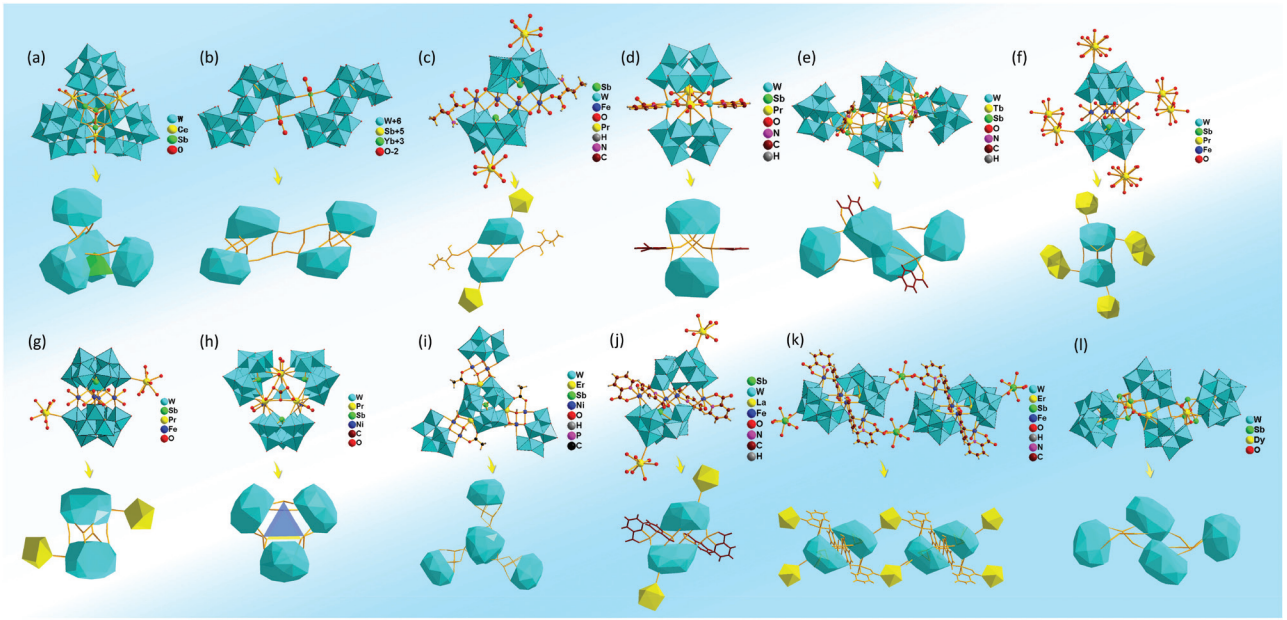

Fig. 1 (a–f) A summary of some representative LnAMTs and OIHLnAMTs.

decorated sandwich-type Fe–Ln heterometallic AMTs $[Ln(H_2O)_8]_2[Fe_4(H_2O)_8(thr)_2][B\text{-}\beta\text{-}SbW_9O_{33}]_2\cdot 22H_2O$ (Ln = Pr^{3+}, Nd^{3+}, Sm^{3+}, Eu^{3+}, Gd^{3+}, Dy^{3+}, Lu^{3+}; thr = threonine) (Fig. 1c).[30] In 2015, Li's group synthesized two kinds of picolinate-decorated LnCAMTs $[Ln_2(H_2O)_4\{WO_2(pic)\}_2(B\text{-}\alpha\text{-}SbW_8O_{30})_2]^{10-}$ (Ln = La^{3+}, Pr^{3+}) and $[\{Ln(H_2O)\}\{Ln(pic)\}(Sb_3O_4)(SbW_8O_{31})(SbW_{10}O_{35})]_2^{24-}$ (Ln = Tb^{3+}, Dy^{3+}, Ho^{3+}) (Fig. 1d and e),[31] and Zhao and co-workers reported two kinds of sandwich-type Fe–Ln heterometallic AMT derivatives $[Pr(H_2O)_8][Pr(H_2O)_6][Fe_4(H_2O)_{10}(B\text{-}\beta\text{-}SbW_9O_{33})_2]\cdot 16H_2O$ and $[Ln(H_2O)_7]_2[Fe_4(H_2O)_{10}(B\text{-}\beta\text{-}SbW_9O_{33})_2]\cdot 22H_2O$ (Ln = Tb^{3+}, Dy^{3+}, Lu^{3+}, Y^{3+}) (Fig. 1f and g).[32] In 2017, Kong and colleagues obtained three $\{Sb_4O_4\}$-bridging Ni–Ln-substituted AMTs $[Ln_3(H_2O)_5Ni(H_2O)_3(Sb_4O_4)(B\text{-}\alpha\text{-}SbW_9O_{33})_3(NiW_6O_{24})(WO_2)_3(CH_3COO)]^{17-}$ (Ln = La^{3+}, Pr^{3+}, Nd^{3+}) and three Ni–Ln heterometallic AMTs $[Ln_3Ni_9(\mu_3\text{-}OH)_9(B\text{-}\alpha\text{-}SbW_9O_{33})_2(B\text{-}\alpha\text{-}PW_9O_{34})_3(CH_3COO)_3]^{30-}$ (Ln = Dy^{3+}, Er^{3+}) by the anionic template strategy (Fig. 1h and i).[33] In 2018–2019, Zhao *et al.* isolated two classes of 2-picolinate-decorated Fe–Ln heterometallic AMTs $[Ln(H_2O)_5]_2[Fe_4(H_2O)_2(pic)_4(B\text{-}\beta\text{-}SbW_9O_{33})_2]^{4-}$ (Ln^{3+} = La^{3+}, Pr^{3+}, Nd^{3+}, Sm^{3+}, Eu^{3+}) and $\{[Ln(H_2O)_6]_2[Fe_4(H_2O)_2(Hpic)_2(pic)_2(B\text{-}\beta\text{-}SbW_9O_{33})_2]\}_2$ (Ln = Gd^{3+}, Dy^{3+}) (Fig. 1j and k),[7] and a group of Ln and Sb-oxo-cluster simultaneously bridging AMTs $\{[Ln_4(H_2O)_6Sb_6O_4](B\text{-}\alpha\text{-}SbW_{10}O_{37})_2(B\text{-}\alpha\text{-}SbW_8O_{31})_2\}^{22-}$ (Ln = Ho^{3+}, Er^{3+}) (Fig. 1l).[34]

Ln-containing materials have aroused increasing research enthusiasm due to their preeminent luminescence properties derived from abundant 4f energy levels, characteristic emission peaks, and long decay lifetimes of Ln^{3+} ions.[35] The sharp emission peaks of Ln ions are the primary cause of high emission color purity and the large Stokes shifts can avoid the interference of the excitation light in the emission light. It has been proved that POT fragments can act as antenna ligands to sensitize the emission of Ln ions,[36–38] which may make LnCPOT materials be applied to the fields of light-emitting diodes, temperature sensors, photoelectric devices, cell imaging techniques, and photodynamic therapy.[39–41] The majority of the previous research reports have been focused on the luminescence studies of homo-Ln containing POTs; however, some problems such as complex device preparation, color imbalance and emission instability will restrict the applications of homo-Ln containing POTs in the optical field.[42–45] To overcome these problems, a useful method is incorporating mixed Ln ions into the POT system to prepare hetero-Ln-codoped POTs. To date, very few examples of hetero-Ln-codoped POTs have been studied.[46] To better investigate the luminescence performances and luminous mechanisms of these materials, various luminescence-tuning strategies such as varying the excitation wavelength, energy transfer (ET) control and controlling the concentration of luminescence centers, and temperature regulation have also been appropriately developed.[47–50] For example, in 2018, Niu *et al.* explored the ET from POT segments to Er^{3+} and Dy^{3+} ions by preparing a class of Dy^{3+}/Er^{3+}-codoped LnCPOTs.[51] In 2019, our group explored the ET mechanism from Tb^{3+} to Eu^{3+} ions conforming to the non-radiative dipole–dipole interaction in the Eu^{3+}/Tb^{3+}-codoped LnCPOT system.[52] The ET studies on different Ln ions in hetero-Ln-codoped POT materials remain underdeveloped.

Herein, we prepared an organic–inorganic hybrid trimeric tri-Tb^{3+}-including an AMT, $Na_{17}\{(WO_4)[Tb(H_2O)(Ac)(B\text{-}\alpha\text{-}SbW_9O_{31}(OH)_2)]_3\}\cdot 50H_2O$ (**Tb_3W_{28}**), in which three $[B\text{-}\alpha\text{-}SbW_9O_{33}]^{9-}$ fragments display a triangle distribution stabilized by a capped $\{WO_4\}$ tetrahedron. The capped tetrahedral $\{WO_4\}$ group plays an important template role in the formation

of $\mathbf{Tb_3W_{28}}$. We successfully utilized Eu^{3+}, Gd^{3+}, and Dy^{3+} ions to substitute Tb^{3+} ions in $\mathbf{Tb_3W_{28}}$ and adjusted the molar ratios of these Ln ions to obtain $\mathbf{Dy_{1.2}Tb_{3\mathit{x}}Gd_{1.8-3\mathit{x}}W_{28}}$ (x = 0, 0.10, 0.20, 0.30, 0.40, 0.50), $\mathbf{Tb_{1.8}Eu_{3\mathit{y}}Gd_{1.2-3\mathit{y}}W_{28}}$ (y = 0, 0.10, 0.14, 0.18, 0.22, 0.26) and $\mathbf{Dy_{1.2}Tb_{3\mathit{z}}Eu_{0.03}Gd_{1.77-3\mathit{z}}W_{28}}$ (z = 0, 0.10, 0.20, 0.30, 0.40) samples (Table S1†). The ET efficiency and mechanism from Dy^{3+} to Tb^{3+} and from Tb^{3+} to Eu^{3+} have been calculated and probed. Moreover, the two-step successive ET process ($Dy^{3+} \rightarrow Tb^{3+} \rightarrow Eu^{3+}$) in the $Eu^{3+}/Tb^{3+}/Dy^{3+}/Gd^{3+}$-codoped $\mathbf{Dy_{1.2}Tb_{3\mathit{z}}Eu_{0.03}Gd_{1.77-3\mathit{z}}W_{28}}$ system was firstly explored. We also tried to tune the emission color by varying the excitation wavelengths for $\mathbf{Dy_{1.2}Tb_{3\mathit{z}}Eu_{0.03}Gd_{1.77-3\mathit{z}}W_{28}}$ (z = 0, 0.10, 0.20, 0.30, 0.40) to obtain a near-white-light emission.

Results and discussion

Structural description

The crystallographic data of $\mathbf{Tb_3W_{28}}$ are illustrated in Table S2.† $\mathbf{Tb_3W_{28}}$ crystallizes in the trigonal space group R_{3m}. The bond valence sum (BVS) calculations suggest that the oxidation states of the O, W, Sb, and Tb centers in $\mathbf{Tb_3W_{28}}$ are −2, +6, +3 and +3, respectively, The BVS value of the O4 atom is 1.20, indicating a possible monoprotonation site (Table S3†). The molecular unit of $\mathbf{Tb_3W_{28}}$ is composed of an acetate-decorated tri-Tb^{3+} containing trimeric $\{(WO_4)[Tb(H_2O)(Ac)(B\text{-}\alpha\text{-}SbW_9O_{31}(OH)_2)]_3\}^{17-}$ ($\mathbf{Tb_3W_{28}}$-**1**) polyoxoanion (POA), 17 Na^+ cations and 50 crystal water molecules. The three-leaf-clover-type structure of $\mathbf{Tb_3W_{28}}$-**1** comprises three trivacant Keggin-type $[B\text{-}\alpha\text{-}SbW_9O_{33}]^{9-}$ ($\{SbW_9\}$) moieties surrounding an acetate-decorated W^{VI}–Tb^{III} heterometallic $\{(WO_4)[Tb(H_2O)(Ac)]_3\}^{4+}$ ($\mathbf{Tb_3W_{28}}$-**2**) group through six W–O–Tb linkers (Fig. 2a–c). Three Sb^{III} heteroatoms in the three $\{SbW_9\}$ subunits are arranged in an equilateral triangle with a side length of 7.625 Å (Fig. 2d). $\mathbf{Tb_3W_{28}}$-**2** contains three $[Tb1(H_2O)]^{3+}$ centers, a capped tetrahedral $\{WO_4\}$ group, and three acetate groups (Fig. 3a). Thereinto, three $Tb1^{3+}$ ions (*i.e.* Tb1, Tb1A, and Tb1B) are also aligned in an equilateral triangle mode (Tb···Tb: 5.884 Å) (Fig. 3b). The $Tb1^{3+}$ ion inhabits an octa-coordinate distorted monocapped square antiprismatic geometry defined by four μ_2-O atoms (O1, O12, O1C, and O12C from two $\{SbW_9\}$ subunits), two carboxyl O atoms (O14 and O19 from one acetate group), one μ_2-O atom (O7 from the capped $\{WO_4\}$ tetrahedron), and one water ligand (O1 W from Tb1), in which the water ligand is located at the cap site of the monocapped square antiprism (Fig. 3c). The Tb–O distances are 2.28(3)–2.44(3) Å and the O–Tb–O bond angles vary from 70.7(7) to 152.5(14)° (Table S4†). Notably, the capped $\{WO_4\}$ tetrahedron is rarely known relative to the common $\{WO_6\}$ octahedron in POT aggregates (Fig. 3d). It is situated on the top of $\mathbf{Tb_3W_{28}}$-**2** and centered in the $\mathbf{Tb_3W_{28}}$-**1** skeleton (Fig. 3e and f). Based on the tetrahedral geometry and the central position, the capped $\{WO_4\}$ tetrahedron may induce the formation of the tri-Tb^{3+} equilateral triangle, further directing the arrangement of three $\{SbW_9\}$ subunits (Fig. 3f). So, the capped $\{WO_4\}$ group may play an important structure-directing agent role in the POA. The three terminal acetate groups act as pendants, linking to three Tb^{3+} ions to increase the space utilization and the structural stability (Fig. 2a).

In addition, Na^+ ions as counter cations and lattice water molecules are distributed in the interspace surrounded by the $\mathbf{Tb_3W_{28}}$-**1** POAs, in which Na^+ ions interact with the $\mathbf{Tb_3W_{28}}$-**1** POAs through strong electrostatic attraction interaction. If Na^+ ions and lattice water molecules are omitted, the supramolecu-

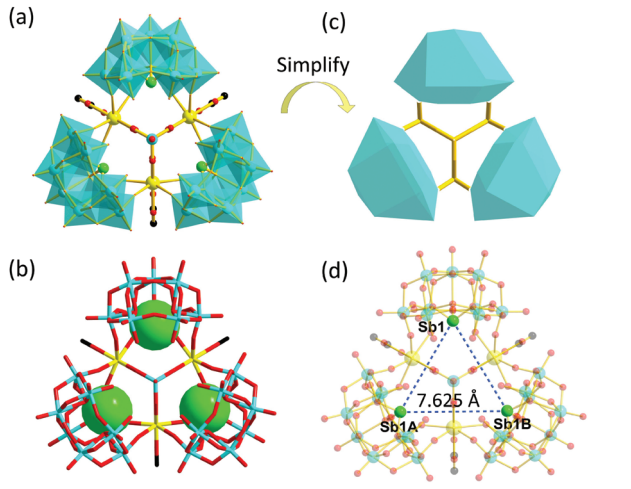

Fig. 2 (a and b) Views of $\mathbf{Tb_3W_{28}}$-**1**; (c) simplified view of $\mathbf{Tb_3W_{28}}$-**1**; and (d) the triangle distribution of Sb1, Sb1A, and Sb1B heteroatoms highlighting the distance of the Sb···Sb heteroatoms. Code: $\{WO_6\}$, purple octahedra; $\{WO_4\}$, blue tetrahedron; O, red spheres; W, blue spheres; Sb, green spheres; Tb, bright yellow spheres; C, black spheres. Symmetry code: A: 1 − x + y, 2 − x, z; B: 2 − y, 1 + x − y, z; C: x, x − y, z.

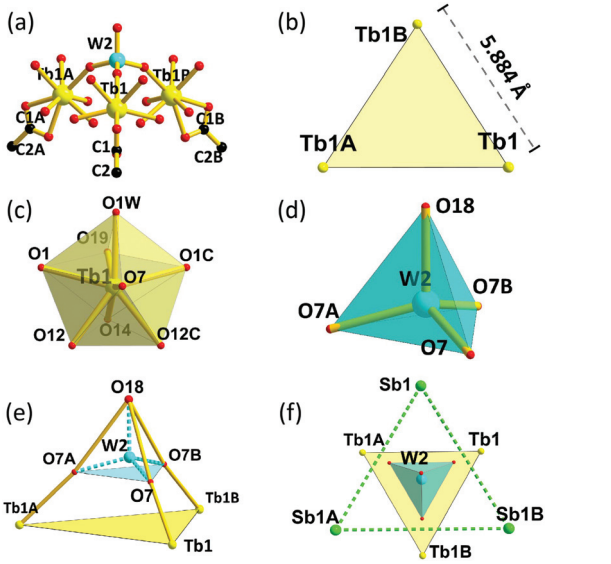

Fig. 3 (a) View of $\mathbf{Tb_3W_{28}}$-**2**; (b) the triangle distribution of Tb1, Tb1A, and Tb1B heteroatoms highlighting the distance of the Tb···Tb ions; (c) the monocapped square antiprismatic geometry of the $Tb1^{3+}$ ions; (d) the capped $\{WO_4\}$ tetrahedron; (e) simplified view of $\mathbf{Tb_3W_{28}}$-**2**; and (f) analysis of $\mathbf{Tb_3W_{28}}$-**1**.

lar 3-D stacking diagram and simplified diagram of the **Tb_3W_{28}-1** POAs show peculiar stacking patterns along the *c* axis. Viewed along the *c* direction, the central **Tb_3W_{28}-1** POA is encircled by neighboring six **Tb_3W_{28}-1** POAs. The six **Tb_3W_{28}-1** POAs are arranged in a hexagonal geometry and take up six vertices of the hexagon. Moreover, the hexagon is encircled by a larger hexagonal geometry including extra twelve **Tb_3W_{28}-1** POAs (Fig. 4a and b). Viewed along the *a* axis, the supramolecular 3-D stacking of the **Tb_3W_{28}-1** POAs and the simplified view demonstrate that the **Tb_3W_{28}-1** POAs are regularly arranged in the mode of –AAA–, every layer is parallel to the adjacent ones. The angle between the *c* axis and these layers is about 60.0° (Fig. 4c and d).

IR spectra and PXRD patterns

Because the radii of Eu^{3+}, Gd^{3+}, Tb^{3+}, and Dy^{3+} ions are close and the cell parameters of **Tb_3W_{28}** are similar to those of our previously reported OIHLnCAMTs $Na_{17}\{(WO_4)[Ln(H_2O)(Ac)(SbW_9O_{31}(OH)_2)]_3\}\cdot 50H_2O$ (Ln = Eu^{3+}, Gd^{3+}, Dy^{3+}),[53] Eu^{3+}, Gd^{3+}, and Dy^{3+} ions can be easily codoped into the host of **Tb_3W_{28}**. The IR spectra and experimental PXRD patterns have been collected to testify the structural consistency of **$Dy_{1.2}Tb_{3x}Gd_{1.8-3x}W_{28}$** ($x$ = 0.00, 0.10, 0.20, 0.30, 0.40, 0.50), **$Tb_{1.8}Eu_{3y}Gd_{1.2-3y}W_{28}$** ($y$ = 0.0, 0.10, 0.14, 0.18, 0.22), and **$Dy_{1.2}Tb_{3z}Eu_{0.03}Gd_{1.77-3z}W_{28}$** ($z$ = 0.00, 0.10, 0.20, 0.30, 0.40) with that of **Tb_3W_{28}**. Moreover, the contents of Dy, Eu, Gd, and Tb elements in the hetero-Ln-codoped samples have also been measured by inductively coupled plasma atomic emission spectrometry (ICP–AES) and the related results are illustrated in Table S1d–f.† As expected, these Ln cations have been successfully codoped. Only the IR spectrum of **Tb_3W_{28}** was discussed (Fig. S1a†). In the low wavenumber region (400–1000 cm^{-1}), four obvious absorption peaks at 686, 788, 887, and 935 cm^{-1} are derived from the stretching vibrations of Sb–O_a, edge-sharing W–O_c, corner-sharing W–O_b, and terminal W–O_t bonds from the $[B\text{-}\alpha\text{-}SbW_9O_{33}]^{9-}$ subunits, respectively.[54] In the middle wavenumber range (1000–2000 cm^{-1}), two absorption peaks at 1462 and 1531 cm^{-1} are attributed to the bending vibrations of C–H bonds and the symmetric stretching vibrations of C–O bonds from acetate ligands. A strong peak at 1632 cm^{-1} originates from the bending vibration of the O–H bond from H_2O molecules.[55–57] In the high wavenumber region (2000–4000 cm^{-1}), a wide absorption band over 3000–3700 cm^{-1} arises from the stretching vibration of the O–H bond of H_2O molecules. The absorption band of the Tb–O bond has not been found due to the prominent ionic interactions between the $[B\text{-}\alpha\text{-}SbW_9O_{33}]^{9-}$ units and Tb^{3+} ions.[58–60] Their IR spectra are identical to those of **Tb_3W_{28}** (Fig. 5a, Fig. S1b and c†), and their experimental PXRD patterns are in good agreement with the simulated PXRD pattern of **Tb_3W_{28}** (Fig. 5b, Fig. S2b and c†). Therefore, all hetero-Ln-codoped samples for measurements are isostructural.

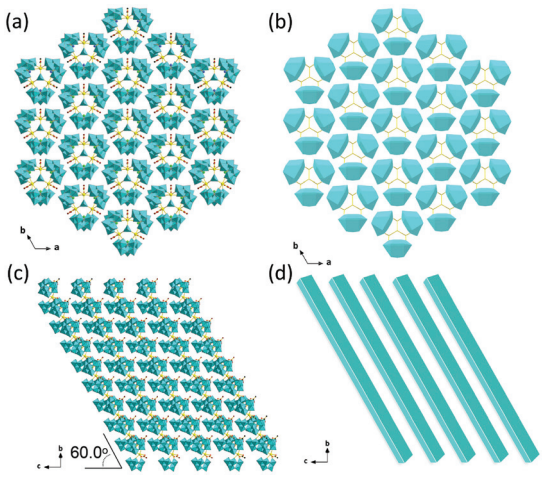

Fig. 4 (a) 3-D stacking pattern for **Tb_3W_{28}-1** along the *c* axis; (b) simplified 3-D stacking pattern for **Tb_3W_{28}-1** along the *c* axis; (c) 3-D stacking pattern for **Tb_3W_{28}-1** along the *a* axis; and (d) simplified 3-D stacking pattern for **Tb_3W_{28}-1** along the *a* axis.

Luminescence studies

ET control and modulation of the molar ratio for hetero-Ln-codoped POT materials can be suggested as convenient and feasible pathways to better understand the luminous mechanism of hetero-Ln-codoped POT materials, thereby to easily realize the emission color tunable properties.[61–64] Some available approaches to confirm the intramolecular ET process between the donor and the acceptor have been developed such as (a) the appearance of excitation bands of the donor in the excitation spectrum obtained by monitoring the emission peak of the acceptor; (b) the overlap between the emission bands of the donor and the excitation bands of the acceptor. In addition, the acceptor can absorb energy from the donor, leading to a decrease of the luminescence emission intensity of the donor, which can also prove the occurrence of ET between the donor and the acceptor.[65,66] Here, based on **Tb_3W_{28}**, various hetero-Ln-codoped samples such as **$Dy_{1.2}Tb_{3x}Gd_{1.8-3x}W_{28}$** ($x$ = 0.00, 0.10, 0.20, 0.30, 0.40, 0.50), **$Tb_{1.8}Eu_{3y}Gd_{1.2-3y}W_{28}$** ($y$ = 0.00, 0.10, 0.14, 0.18, 0.22, 0.26), and **$Dy_{1.2}Tb_{3z}Eu_{0.03}Gd_{1.77-3z}W_{28}$** ($z$ = 0.00, 0.10, 0.20, 0.30, 0.40) have been prepared. Their emission and excitation spectra and lifetime decay curves have been measured to calculate the ET efficiency and analyze the ET mechanisms among Dy^{3+}, Tb^{3+}, and Eu^{3+} ions. Notably, because the Gd^{3+} ion cannot display an emission band in the range of 430–750 nm under excitation with UV light,[67] it was introduced as a doping component to adjust the molar ratio of Dy^{3+}, Tb^{3+}, and Eu^{3+} ions according to our research requirement.

To explore the ET phenomenon among Dy^{3+}, Tb^{3+}, and Eu^{3+} ions, the excitation spectra of **$Dy_{1.2}Tb_{0.3}Gd_{1.5}W_{28}$**, **$Tb_{1.8}Eu_{0.3}Gd_{0.9}W_{28}$**, and **$Tb_3W_{28}$** have been collected by monitoring different emission lights. When monitoring the Tb^{3+} $^5D_4 \rightarrow {}^7F_5$ emission at 545 nm, the excitation spectrum of **$Dy_{1.2}Tb_{0.3}Gd_{1.5}W_{28}$** shows six Dy^{3+} excitation peaks at 352, 366, 389, 426, 455, and 476 nm ($^6H_{15/2} \rightarrow {}^6P_{7/2}$, $^6P_{5/2}$, $^4I_{13/2}$, $^4G_{11/2}$, $^4I_{15/2}$, and $^4F_{9/2}$), respectively, and a Tb^{3+} obvious excitation peak at 489 nm ($^7F_6 \rightarrow {}^5D_4$) (Fig. 5c), which suggests the occurrence of ET_1 from Dy^{3+} ions to Tb^{3+} ions for

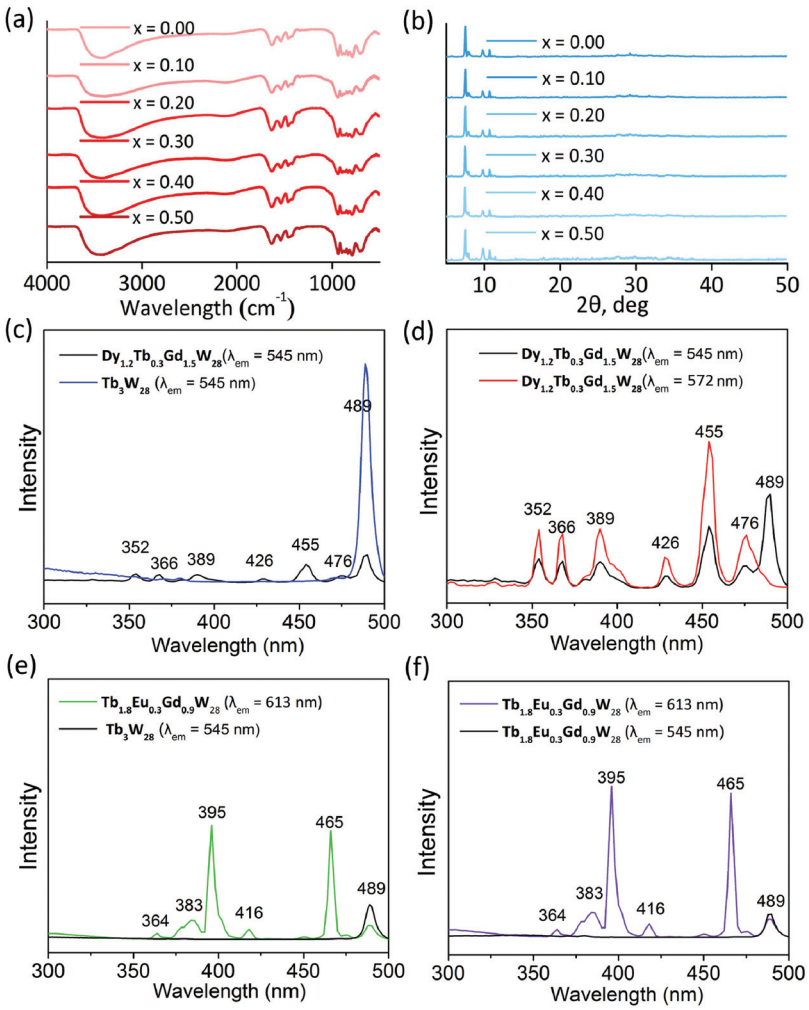

Fig. 5 (a) IR spectra of $Dy_{1.2}Tb_{3x}Gd_{1.8-3x}W_{28}$ (x = 0, 0.10, 0.20, 0.30, 0.40, 0.50); (b) experimental PXRD patterns of $Dy_{1.2}Tb_{3x}Gd_{1.8-3x}W_{28}$ (x = 0, 0.10, 0.20, 0.30, 0.40, 0.50); (c) comparison of the excitation spectra of $Dy_{1.2}Tb_{0.3}Gd_{1.5}W_{28}$ and Tb_3W_{28} while monitoring the emission peak at 545 nm; (d) comparison of the excitation spectra of $Dy_{1.2}Tb_{0.3}Gd_{1.5}W_{28}$ while monitoring the emission peaks at 545 and 572 nm; (e) comparison of the excitation spectra of $Tb_{1.8}Eu_{0.3}Gd_{0.9}W_{28}$ (λ_{em} = 613 nm) and Tb_3W_{28} (λ_{em} = 545 nm); and (f) comparison of the excitation spectra of $Tb_{1.8}Eu_{0.3}Gd_{0.9}W_{28}$ (λ_{em} = 613 and 545 nm).

$Dy_{1.2}Tb_{0.3}Gd_{1.5}W_{28}$.[68] However, when monitoring the Dy^{3+} $^4F_{9/2}$ → $^6H_{13/2}$ emission at 572 nm, the excitation spectrum of $Dy_{1.2}Tb_{0.3}Gd_{1.5}W_{28}$ only exhibits six Dy^{3+}excitation peaks at 352, 366, 389, 426, 455, and 476 nm and no Tb^{3+} excitation peak is observed, which illustrates that the ET from Tb^{3+} ions to Dy^{3+} ions does not occur in $Dy_{1.2}Tb_{0.3}Gd_{1.5}W_{28}$ (Fig. 5d). Similarly, when monitoring the Eu^{3+} $^5D_0$ → $^7F_2$ emission at 613 nm, $Tb_{1.8}Eu_{0.3}Gd_{0.9}W_{28}$ presents five Eu^{3+} excitation peaks ($^7F_0$ → $^5D_4$, $^5L_7$, $^5L_6$, $^5D_3$, $^5D_2$) at 364, 383, 395, 416, and 465 nm, respectively, and a Tb^{3+} excitation peak ($^7F_6$ → $^5D_4$) at 489 nm (Fig. 5e),[69,70] where the appearance of the peak of Tb^{3+} ions at 489 nm indicates that the Tb^{3+} ions can transfer energy to Eu^{3+} ions (ET_2). However, when monitoring the Tb^{3+} $^5D_4$ → $^7F_5$ emission at 545 nm, $Tb_{1.8}Eu_{0.3}Gd_{0.9}W_{28}$ only shows an excitation peak of Tb^{3+} ions at 489 nm and does not display any excitation peaks of Eu^{3+} ions, which demonstrates the absence of ET_2 from Eu^{3+} ions to Tb^{3+} ions (Fig. 5f). Therefore, the ET_1 process from Dy^{3+} ions to Tb^{3+} ions for $Dy_{1.2}Tb_{0.3}Gd_{1.5}W_{28}$ and the ET_2 process from Tb^{3+} ions to Eu^{3+} ions for $Tb_{1.8}Eu_{0.3}Gd_{0.9}W_{28}$ will be studied in detail.

The ET process from the donor to the acceptor often gives rise to the decline of the emission intensity and the shortening of the decay lifetime of the donor.[71] To explore the ET_1 process from Dy^{3+} ions to Tb^{3+} ions, under the Dy^{3+} $^6H_{15/2}$ → $^4I_{13/2}$ excitation at 389 nm, the emission spectra and decay lifetime curves of the emission peak at 572 nm for $Dy_{1.2}Tb_{3x}Gd_{1.8-3x}W_{28}$ have been measured. As shown in Fig. 6a, the emission spectrum of $Dy_{1.2}Gd_{1.8}W_{28}$ displays three f–f emission peaks of Dy^{3+} ions at 484, 572, and 660 nm, which are attributed to the f–f $^4F_{9/2}$ → ^6H_K (K = 15/2, 13/2, 11/2) transitions, respectively,[68] and the emission spectra of $Dy_{1.2}Tb_{3x}Gd_{1.8-3x}W_{28}$ (x = 0.10, 0.20, 0.30, 0.40, 0.50) generate four dominant emission peaks of Tb^{3+} at 489, 545, 582, and 623 nm corresponding to the $^5D_4$ → ^7F_J (J = 6, 5, 4, 3) tran-

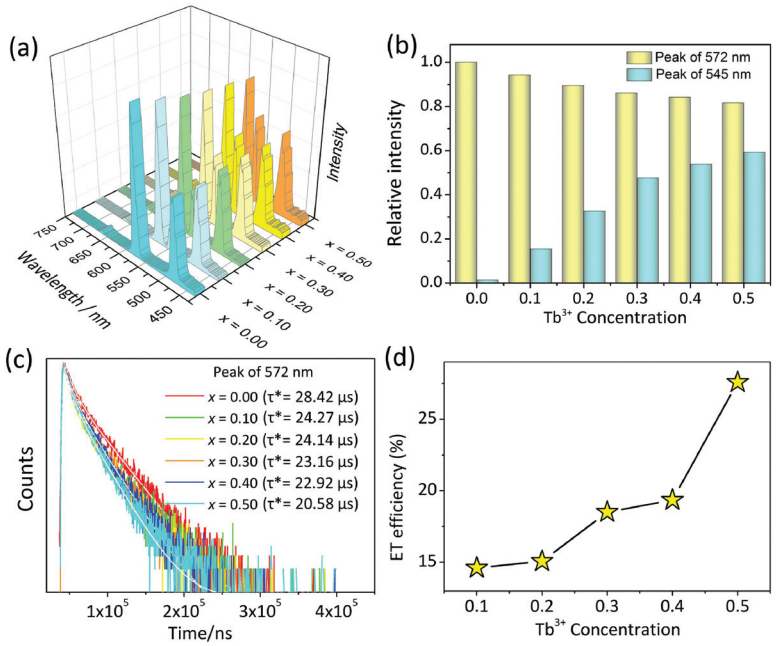

Fig. 6 (a) Emission spectra of $Dy_{1.2}Tb_{3x}Gd_{1.8-3x}W_{28}$ (x = 0.00, 0.10, 0.20, 0.30, 0.40, 0.50) obtained at λ_{ex} = 389 nm; (b) dependence of the emission intensity of the peaks at 545 and 572 nm on the concentration of Tb^{3+} ions at λ_{ex} = 389 nm; (c) lifetime decay curves of the peaks at 572 nm for $Dy_{1.2}Tb_{3x}Gd_{1.8-3x}W_{28}$ (x = 0.00, 0.10, 0.20, 0.30, 0.40, 0.50) at λ_{ex} = 389 nm; and (d) dependence of ET_1 efficiency ($Dy^{3+} \rightarrow Tb^{3+}$) on the concentration of Tb^{3+} ions at λ_{ex} = 389 nm for $Dy_{1.2}Tb_{3x}Gd_{1.8-3x}W_{28}$.

sitions as well as the emission peaks of Dy^{3+}.[70] When the molar concentration for Dy^{3+} ions is fixed as 0.40 and the molar concentration of Tb^{3+} ions increases from 0.00 to 0.50, the Dy^{3+} $^6H_{15/2} \rightarrow {}^4I_{13/2}$ emission intensity of the peak at 572 nm gradually decreases (Fig. 6a and b). In addition, the decay lifetime of the emission peak at 572 nm declines from 28.42 to 20.58 μs (Fig. 6c and Table S5†). The above-mentioned observation demonstrates that ET_1 from Dy^{3+} ions to Tb^{3+} ions results in a decline of the emission intensity of Dy^{3+} ions as the concentration of Tb^{3+} ions increases. Eqn (1) can be given as:[72,73]

$$\eta_{ET} = 1 - \tau_S/\tau_{S0} \quad (1)$$

where η_{ET} is the ET_1 efficiency, τ_S and τ_{S0} are, respectively, the decay lifetimes of the emission peaks at 572 nm derived from the $^6H_{15/2} \rightarrow {}^4I_{13/2}$ transition of Dy^{3+} ions (the donor) with and without Tb^{3+} ions (the acceptor). The ET_1 efficiency η_{Dy-Tb} values in $Dy_{1.2}Tb_{3x}Gd_{1.8-3x}W_{28}$ (x = 0.10, 0.20, 0.30, 0.40, 0.50) are, respectively, 14.60, 15.06, 18.51, 19.35, and 27.59% (Fig. 6d). Apparently, as the concentration of Tb^{3+} ions increases, the ET_1 efficiency also increases.

Currently, there are two major ET mechanisms: electric exchange interaction (R_c < 5.0 Å) and electric multipolar interaction (R_c > 5.0 Å). R_c is the critical distance of the ET from the donor to the acceptor. To determine the ET_1 mechanism between Dy^{3+} and Tb^{3+}, the average distance (R_{Dy-Tb}) of the ET from the donor to the acceptor has been calculated using eqn (2):[74,75]

$$R_{Dy-Tb} = 2 \times [3V/(4\pi\chi Z)]^{1/3} \quad (2)$$

in which V stands for the volume of a unit cell, χ represents the total molar concentration of Dy^{3+} and Tb^{3+} ions, and Z (Z = 9) is the number of the Dy^{3+} donors in the host (Fig. S3†). The R_{Dy-Tb} values of $Dy_{1.2}Tb_{3x}Gd_{1.8-3x}W_{28}$ (x = 0.10, 0.20, 0.30, 0.40, and 0.50) are 17.4, 16.39, 15.57, 14.89, and 12.93 Å, respectively. All the R_{Dy-Tb} values are larger than the critical distance (5.0 Å) of the electric exchange interaction, demonstrating that the electric multipolar interaction can be responsible for the main ET_1 mechanism from Dy^{3+} ions to Tb^{3+} ions.

In line with Dexter's expression for the electric multiple interactions, eqn (3) can be used:[76,77]

$$I_{S0}/I_S \propto C^{n/3} \quad (3)$$

where I_{S0} and I_S are respectively the emission intensities of the peak at 572 nm (the $^6H_{15/2} \rightarrow {}^4I_{13/2}$ transition of Dy^{3+} ions) in the absence and presence of Tb^{3+} ions for $Dy_{1.2}Tb_{3x}Gd_{1.8-3x}W_{28}$, C is the total molar concentration of Dy^{3+} and Tb^{3+}, and n = 6, 8, and 10, respectively, represent the electric dipole–dipole interaction, the electric dipole–quadrupole interaction, and the electric quadrupole–quadrupole interaction. Through the linear fitting using eqn (3), it can be observed that the relative agreement factor R^2 values are severally 0.94151 (n = 6), 0.91703 (n = 8), and 0.87583 (n = 10), which indicates that the electric multipolar mechanism from Dy^{3+} to Tb^{3+} ions in $Dy_{1.2}Tb_{3x}Gd_{1.8-3x}W_{28}$ (x = 0.10, 0.20, 0.30, 0.40, 0.50) is a nonradiative dipole–dipole interaction (Fig. 7).

To investigate the ET_2 process from Tb^{3+} to Eu^{3+} ions, based on the $^7F_6 \rightarrow {}^5L_{10}$ excitation of Tb^{3+} at 370 nm,[70] the emission spectra and lifetime decay curves of the emission

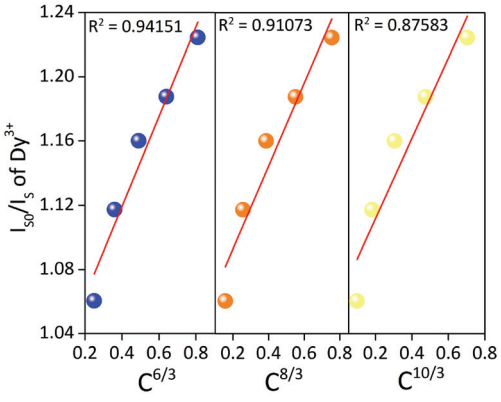

Fig. 7 Dependence of I_{S0}/I_0 of the $^6H_{15/2} \rightarrow {}^4I_{13/2}$ transition from Dy^{3+} ions on $C^{6/3}$, $C^{8/3}$, and $C^{10/3}$.

peak at 545 nm for $\mathbf{Tb_{1.8}Eu_{3y}Gd_{1.2-3y}W_{28}}$ (y = 0.0, 0.1, 0.14, 0.18, 0.22, 0.26) have been collected. As shown in Fig. S4a,† the emission spectrum of $\mathbf{Tb_{1.8}Gd_{1.2}W_{28}}$ reveals four f–f emission peaks at 489, 545, 582, and 623 nm owing to the $^5D_4 \rightarrow {}^7F_K$ (K = 6, 5, 4, 3) transitions of Tb^{3+} ions, respectively, and the emission spectra of $\mathbf{Tb_{1.8}Eu_{3y}Gd_{1.2-3y}W_{28}}$ (y = 0.10, 0.14, 0.18, 0.22, 0.26) show five featured f–f emission peaks at 580, 594, 613, 653, and 700 nm derived from the $^5D_0 \rightarrow {}^7F_J$ (J = 0, 1, 2, 3, 4) transitions of Eu^{3+} ions, respectively, as well as four emission peaks of Tb^{3+} ions.[69,70] When the molar concentration is fixed as 0.60 for Tb^{3+} ions, and increases from 0.00 to 0.26 for Eu^{3+} ions, the emission intensity of Tb^{3+} ions at 545 nm decreases gradually (Fig. S4a and b†). By monitoring the $^5D_4 \rightarrow {}^7F_5$ emission peak of Tb^{3+} ions at 545 nm, the decay lifetimes are also observed to decrease from 256.57 to 75.02 μs (Fig. S4c and Table S6†), which illustrates the occurrence of ET_2 from Tb^{3+} ions to Eu^{3+} ions. According to eqn (1), the η_{Tb-Eu} values for $\mathbf{Tb_{1.8}Eu_{3y}Gd_{1.2-3y}W_{28}}$ (y = 0.10, 0.14, 0.18, 0.22, 0.26) are respectively 49.03, 52.06, 65.39, 69.56, and 70.76% (Fig. S4d†). It is clearly seen that the ET_2 efficiency also increases as the concentration of Tb^{3+} ions increases. Furthermore, in accordance with eqn (2), the R_{Tb-Eu} values of $\mathbf{Tb_{1.8}Eu_{3y}Gd_{1.2-3y}W_{28}}$ (y = 0.10, 0.14, 0.18, 0.22, 0.26) are 15.57, 15.28, 15.01, 14.77, and 14.45 Å, which are all larger than the critical distance (5.0 Å) of the electric exchange interaction. Thus, the electric multipolar interaction is also the primary ET_2 mechanism from Tb^{3+} ions to Eu^{3+} ions. Through the linear fitting by using eqn (3), the R^2 values are 0.93882 (n = 6), 0.94717, (n = 8), and 0.95447 (n = 10), which demonstrates that the multipolar mechanism from Tb^{3+} ions to Eu^{3+} ions in $\mathbf{Tb_{1.8}Eu_{3y}Gd_{1.2-3y}W_{28}}$ (y = 0.10, 0.14, 0.18, 0.22, 0.26) is a nonradiative quadrupole–quadrupole interaction (Fig. S5†).

From the above-mentioned analyses about the ET_1 process from Dy^{3+} ions to Tb^{3+} ions and the ET_2 process from Tb^{3+} ions to Eu^{3+} ions, it can be speculated that Tb^{3+} ions can act as not only the energy acceptor of Dy^{3+} ions but also the energy donor of Eu^{3+} ions in the $Dy^{3+}/Tb^{3+}/Eu^{3+}$-doped system, theoretically, generating a two-step successive $Dy^{3+} \rightarrow Tb^{3+} \rightarrow Eu^{3+}$ ET_3 process. To attest this hypothesis, the emission spectra and lifetime decay curves of $\mathbf{Dy_{1.2}Tb_{3z}Eu_{0.03}Gd_{1.77-3z}W_{28}}$ (z = 0, 0.10, 0.20, 0.30, 0.40) have been measured. As shown in Fig. 8a, under the $^6H_{15/2} \rightarrow {}^4I_{13/2}$ excitation of Dy^{3+} at 389 nm, the emission spectra of $\mathbf{Dy_{1.2}Tb_{3z}Eu_{0.03}Gd_{1.77-3z}W_{28}}$ give birth to the simultaneous f–f emission peaks of Dy^{3+}, Tb^{3+}, and Eu^{3+} ions. Under the conditions of the molar concentrations of Dy^{3+} and Eu^{3+} ions being fixed as 0.40 and 0.01, severally, as the molar concentration of Tb^{3+} ions increases from 0 to 0.40, the emission intensity of the Dy^{3+} $^6H_{15/2} \rightarrow {}^4I_{13/2}$ emission peak at 572 nm declines gradually (Fig. 8b), and the decay lifetimes of the emission peak at 572 nm also decrease from 16.46 to 7.74 μs (Fig. S6a and Table S7†), indicating that the Tb^{3+} ions can absorb energy from Dy^{3+} ions by a nonradiative relaxation. Notably, at z = 0 and 0.10, the lifetime decay curves of the emission peak at 572 nm conform to the monoexponential behavior, indicating that the emission peak at 572 nm is mainly derived from the contribution of Dy^{3+} ions (Table S7†). However, at z = 0.20, 0.30, and 0.40, the lifetimes decay curves of the emission peak at 572 nm accord with the double-exponential behavior, illustrating that the emission peak at 572 nm is mainly owing to the common contribution of Dy^{3+} and Tb^{3+} ions (Table S7†). Furthermore, due to the molar concentration of Eu^{3+} ions being fixed at 0.01, the $^5D_0 \rightarrow {}^7F_2$ emission peak intensity at 613 nm of Eu^{3+} ions gradually increases and the decay lifetime of the emission peak at 613 nm of Eu^{3+} ions is prolonged from 126.85 to 719.84 μs (Fig. S6b and Table S8†) upon increasing the molar concentration of Tb^{3+} ions (Fig. 8b), which illustrates the occurrence of ET from Tb^{3+} ions to Eu^{3+} ions. Summarizing, the two-step successive $Dy^{3+} \rightarrow Tb^{3+} \rightarrow Eu^{3+}$ ET_3 process occurs in $\mathbf{Dy_{1.2}Tb_{3z}Eu_{0.03}Gd_{1.77-3z}W_{28}}$ under excitation at 389 nm. The two-step successive $Dy^{3+} \rightarrow Tb^{3+} \rightarrow Eu^{3+}$ ET_3 process has been interpreted in the schematic energy level diagram (Fig. 8c). Under excitation at 389 nm, the electrons at the ground state ($^6H_{15/2}$) of Dy^{3+} ions jump to the $^4I_{13/2}$ excited state and relax to the $^4F_{9/2}$ state by the nonradiative transition, promoting the f–f $^4F_{9/2} \rightarrow {}^6H_K$ (K = 15/2, 13/2, 11/2) emission transitions of Tb^{3+} ions. Meanwhile, part of the energy at the $^4F_{9/2}$ state of Dy^{3+} ions migrates to the $^5D_4$ state of Tb^{3+} ions due to the overlap between the $^4F_{9/2}$ state (2.57 eV) of Dy^{3+} ions and the $^5D_4$ state (2.54 eV) of Tb^{3+} ions, leading to the $^5D_4 \rightarrow {}^7F_J$ (J = 6, 5, 4, 3) emission transitions of Tb^{3+} ions. Because of the overlap between the $^5D_4$ state (2.54 eV) of Tb^{3+} ions and the $^5D_1$ state (2.32 eV) of Eu^{3+} ions, part energy at the $^5D_4$ state of Tb^{3+} ions shifts to the $^5D_1$ state of Eu^{3+}, triggering the $^5D_0 \rightarrow {}^7F_J$ (J = 0, 1, 2, 3, 4) emission transitions.

The CIE diagram 1931 is a high-quality pathway to understand the authenticity of emission colours, which involves some important optical parameters such as chromaticity coordinate, dominant wavelength, colour purity, and correlated colour temperature (CCT). The chromaticity coordinate represents the actual luminous colour of an emitter. The colour defined by the dominant wavelength is consistent with the actual luminous colour of a luminescent material in theory.

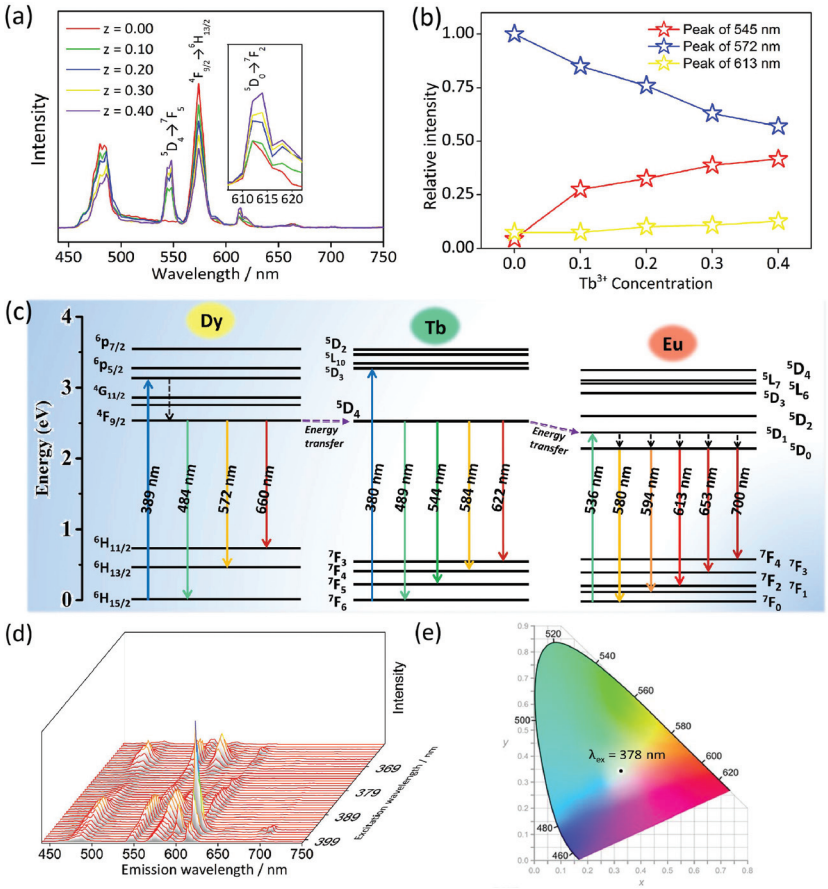

Fig. 8 (a) Emission spectra of $Dy_{1.2}Tb_{3z}Eu_{0.03}Gd_{1.77-3z}W_{28}$ (z = 0.00, 0.10, 0.20, 0.30, 0.40) obtained at λ_{ex} = 389 nm; (b) dependence of the emission intensity of peaks at 545, 572, and 613 nm on the concentration of Tb^{3+} ions at λ_{ex} = 389 nm; (c) schematic energy-level diagram showing the two-step successive $Dy^{3+} \rightarrow Tb^{3+} \rightarrow Eu^{3+}$ ET process (the solid line is the radiation transition and the dotted line is the non-radiative transition); (d) emission spectra of $Dy_{1.2}Tb_{1.2}Eu_{0.03}Gd_{0.57}W_{28}$ at various excitation wavelengths (360–400 nm); and (e) the CIE 1931 diagram of $Dy_{1.2}Tb_{1.2}Eu_{0.03}Gd_{0.57}W_{28}$ upon excitation at 378 nm.

Colour purity stands for the brightness of the colour and is usually calculated using eqn (4):

$$\text{colour purity} = [(x - x_i)^2 + (y - y_i)^2/(x_d - x_i)^2 + (y_d - y_i)^2]^{1/2} \quad (4)$$

in which (x, y), (x_d, y_d) and (x_i, y_i) are the chromaticity coordinates of the light source, the dominant wavelength, and the white light (0.3333, 0.3333), respectively.

CCT represents the warmth of a light source, which is divided into warm (<3000 K), standard (3000–5000 K) and cold (>5000 K). CCT can be calculated using eqn (5):

$$CT = 499.0n^3 + 3525.0n^2 + 6823.3n + 5520.22 \quad (5)$$

in which $n = (x - x_e)/(y_e - y)$; (x_e, y_e) are the epicenter coordinates (0.3320, 0.1858).[78–82]

To verify the emission colour-tunable properties, the emission spectra of $Dy_{1.2}Tb_{3z}Eu_{0.03}Gd_{1.77-3z}W_{28}$ (z = 0.10, 0.20, 0.30, 0.40) have been measured by switching the excitation wavelength from 360 to 400 nm (Fig. 8d and Fig. S7a–c†). It can be observed that under different excitations, most of the emission colors are concentrated on blue and green whereas a few cases are yellow and orange for $Dy_{1.2}Tb_{3z}Eu_{0.03}Gd_{1.77-3z}W_{28}$ (Fig. S8a–d and Tables S9–S12†). It should be pointed out that $Dy_{1.2}Tb_{1.2}Eu_{0.03}Gd_{0.57}W_{28}$ can emit a near-white light with the chromaticity coordinates of (0.32837, 0.34187) and a cool CCT of 5678 K under excitation at 378 nm (Fig. 8e and Table S12†), which may show its good potential to act as a white light emitter.

Conclusions

In summary, the synthesis of an organic–inorganic hybrid tri-Tb^{3+}-substituted trimeric AMT Tb_3W_{28} demonstrates that the capped $\{WO_4\}$ tetrahedron plays an important template role in controlling the formation of Tb_3W_{28}. When Eu^{3+}, Gd^{3+}, and Dy^{3+} ions were codoped into Tb_3W_{28}, the $Eu^{3+}/Tb^{3+}/Dy^{3+}/Gd^{3+}$-codoped samples can still maintain the structure of Tb_3W_{28}. Under the $^6H_{15/2} \rightarrow {}^4I_{13/2}$ excitation of Dy^{3+} ions at 389 nm, the ET_1 mechanism ($Dy^{3+} \rightarrow Tb^{3+}$) has been confirmed as a non-radiative dipole–dipole interaction. Based on the $^7F_6 \rightarrow {}^5L_{10}$

excitation of Tb^{3+} ions at 380 nm, the ET_2 mechanism ($Tb^{3+} \rightarrow Eu^{3+}$) is a non-radiative quadrupole–quadrupole interaction. Moreover, under the $^6H_{15/2} \rightarrow {}^4I_{13/2}$ excitation of Dy^{3+} ions at 389 nm, the two-step successive $Dy^{3+} \rightarrow Tb^{3+} \rightarrow Eu^{3+}$ ET_3 process has occurred. Through switching the excitation wavelength for $\mathbf{Dy_{1.2}Tb_{3z}Eu_{0.03}Gd_{1.77-3z}W_{28}}$, the tunable emission colours from blue to yellow have been realized. Under excitation at 378 nm, $\mathbf{Dy_{1.2}Tb_{1.2}Eu_{0.03}Gd_{0.57}W_{28}}$ generates a near-white-light emission. This work not only provides a systematic ET mechanism study about hetero-Ln-codoped AMTs, but also offers some useful guidance for designing novel performance-oriented Ln-codoped POM-based materials. In the future, we will make great efforts to realize the lighting technology using hetero-Ln-codoped POT materials.

Conflicts of interest

There are no conflicts to declare.

Acknowledgements

This work was supported by the National Natural Science Foundation of China (21671054, 21771052, 21871077, and 21571048), the Program for Innovation Teams in Science and Technology in Universities of Henan Province (20IRTSTHN004), and the Program of First-Class Discipline Cultivation Project of Henan University (2019YLZDYJ02 and CJ1205A0240019).

Notes and references

1 A. Blazevic and A. Rompel, *Coord. Chem. Rev.*, 2016, **307**, 42.
2 Y.-W. Li, L.-Y. Guo, H.-F. Su, M. Jagodič, M. Luo, X.-Q. Zhou, S.-Y. Zeng, C.-H. Tung and D. Sun, *Inorg. Chem.*, 2017, **56**, 2481.
3 J. C. Liu, J. Luo, Q. Han, J. Cao, L. J. Chen, Y. Song and J. W. Zhao, *J. Mater. Chem. C*, 2017, **5**, 2043.
4 M. Raula, O. G. Gan, M. Saganovich, O. Zeiri, Y. Wang, M. R. Chierotti, R. Gobetto and I. A. Wenstock, *Angew. Chem., Int. Ed.*, 2015, **54**, 12416.
5 Q. Zheng, L. Vila-Nadal, Z. Lang, J.-J. Chen, D.-L. Long, J. S. Mathieson, J. M. Poblet and L. Cronin, *J. Am. Chem. Soc.*, 2018, **140**, 2595.
6 P. Ma, F. Hu, J. Wang and J. Niu, *Coord. Chem. Rev.*, 2019, **378**, 281.
7 Y. H. Chen, L. H. Sun, S. Z. Chang, L. J. Chen and J. W. Zhao, *Inorg. Chem.*, 2018, **57**, 15079.
8 J.-C. Liu, Q. Han, L.-J. Chen, J.-W. Zhao, C. Streb and Y.-F. Song, *Angew. Chem., Int. Ed.*, 2018, **57**, 8416.
9 M. Ibrahim, V. Mereacre, N. Leblanc, W. Wernsdorfer, C. E. Anson and A. K. Powell, *Angew. Chem., Int. Ed.*, 2015, **54**, 15574.
10 X.-Y. Zheng, Y.-H. Jiang, G.-L. Zhuang, D.-P. Liu, H.-G. Liao, X.-J. Kong, L.-S. Long and L.-S. Zheng, *J. Am. Chem. Soc.*, 2017, **139**, 18178.
11 F. Xu, H. N. Miras, R. A. Scullion, D.-L. Long, J. Thiel and L. Cronin, *Proc. Natl. Acad. Sci. U. S. A.*, 2012, **109**, 11609.
12 B. K. Teo and N. J. A. Sloane, *Inorg. Chem.*, 1985, **24**, 4545.
13 S. S. Wang and G. Y. Yang, *Chem. Rev.*, 2015, **115**, 4893.
14 S. X. Shang, Z. G. Lin, A. X. Yin, S. Yang, Y. N. Chi, Y. Wang, J. Dong, B. Liu, N. Zhen, C. L. Hill and C. W. Hu, *Inorg. Chem.*, 2018, **57**, 8831.
15 R. Gupta, I. Khan, F. Hussain, A. M. Bossoh, I. M. Mbomekalle, P. Oliveira, M. Sadakane, C. Kato, K. Ichihashi, K. Inoue and S. Nishihara, *Inorg. Chem.*, 2017, **56**, 8759.
16 C. Ritchie, E. G. Moore, M. Speldrich, P. Kögerler and C. Boskovic, *Angew. Chem., Int. Ed.*, 2010, **49**, 7702.
17 Q. Han, J.-C. Liu, Y. Wen, L.-J. Chen, J.-W. Zhao and G.-Y. Yang, *Inorg. Chem.*, 2017, **56**, 7257.
18 J. W. Zhao, H. L. Li, Y. Z. Li, C. Y. Li, Z. L. Wang and L. J. Chen, *Cryst. Growth Des.*, 2014, **14**, 5495.
19 P. Yang, W. Zhao, A. Shkurenko, Y. Belmabkhout, M. Eddaoudi, X. Dong, H. N. Alshareef and N. M. Khashab, *J. Am. Chem. Soc.*, 2019, **141**, 1847.
20 H. N. Miras, J. Yan, D. L. Long and L. Cronin, *Chem. Soc. Rev.*, 2012, **41**, 7403.
21 D.-L. Long, H. Abbas, P. Kögerler and L. Cronin, *J. Am. Chem. Soc.*, 2004, **126**, 13880.
22 C. P. Pradeep, D. L. Long, C. Streb and L. Cronin, *J. Am. Chem. Soc.*, 2008, **130**, 14946.
23 J. L. Liu, M. T. Jin, L. J. Chen and J. W. Zhao, *Inorg. Chem.*, 2018, **57**, 12509.
24 B. Nohra, P. Mialane, A. Dolbecq, E. Rivière, J. Marrot and F. Sécheresse, *Chem. Commun.*, 2009, **40**, 2703.
25 S. Reinoso, *Dalton Trans.*, 2011, **40**, 6610.
26 T. Yamase, H. Naruke and Y. Sasaki, *J. Chem. Soc., Dalton Trans.*, 1990, 1687.
27 M. Ibrahim, S. S. Mal, B. S. Bassil, A. Banerjee and U. Kortz, *Inorg. Chem.*, 2011, **50**, 956.
28 G. Xue, J. Vaissermann and P. Gouzerh, *J. Cluster Sci.*, 2002, **13**, 409.
29 A. H. Ismail, B. S. Bassil, I. Römer and U. Kortz, *Z. Anorg. Allg. Chem.*, 2013, **639**, 2510.
30 J.-W. Zhao, J. Cao, Y.-Z. Li, J. Zhang and L.-J. Chen, *Cryst. Growth Des.*, 2014, **14**, 62179.
31 L.-L. Li, H.-Y. Han, Y.-H. Wang, H.-Q. Tan, H.-Y. Zang and Y.-G. Li, *Dalton Trans.*, 2015, **44**, 11429.
32 L. Chen, J. Cao, X. Li, X. Ma, J. Luo and J. Zhao, *CrystEngComm*, 2015, **17**, 5002.
33 J. Cai, X. Y. Zheng, J. Xie, Z. H. Yan, X. J. Kong, Y. P. Ren, L. S. Long and L. S. Zheng, *Inorg. Chem.*, 2017, **56**, 8439.
34 X. Xu, Y. H. Chen, Y. Zhang, Y. F. Liu, L. J. Chen and J. W. Zhao, *Inorg. Chem.*, 2019, **58**, 11636.
35 F. A. Almeida Paz, J. Klinowski, S. M. F. Vilela, J. P. C. Tome, J. A. S. Cavaleiro and J. Rocha, *Chem. Soc. Rev.*, 2012, **41**, 1088.

36 S. V. Eliseeva and J.-C. G. Bunzli, *Chem. Soc. Rev.*, 2010, **39**, 189.
37 W. Zhou, M. Gu, Y. Ou, C. Zhang, X. Zhang, L. Zhou and H. Liang, *Inorg. Chem.*, 2017, **56**, 7433.
38 B. P. Kore, A. Kumar, A. Pandey, R. E. Kroon, J. J. Terblans, S. J. Dhoble and H. C. Swart, *Inorg. Chem.*, 2017, **56**, 4996.
39 J.-W. Zhao, Y.-Z. Li, L.-J. Chen and Y.-Y. Guo, *Chem. Commun.*, 2016, **52**, 4418.
40 L. Armelaoa, S. Quici, F. Barigelletti, G. Accorsi, G. Bottaro, M. Cavazzini and E. Tondelloe, *Coord. Chem. Rev.*, 2010, **254**, 487.
41 J. N. Hao, X.-Y. Xu, X. Lian, C. Zhang and B. Yan, *Inorg. Chem.*, 2017, **56**, 11176.
42 X. Mi, D. Sheng, Y. Yu, Y. Wang, L. Zhao, J. Lu, Y. Li, D. Li, J. Dou, J. Duan and S. Wang, *ACS Appl. Mater. Interfaces*, 2019, **11**, 7914.
43 Q.-Y. Yang, M. Pan, S.-C. Wei, K. Li, B.-B. Du and C.-Y. Su, *Inorg. Chem.*, 2015, **54**, 5707.
44 R. An, H. Zhao, H.-M. Hu, X. Wang, M.-L. Yang and G. Xue, *Inorg. Chem.*, 2016, **55**, 871.
45 F. Kang, G. Sun, A. Wang, X. Xiao, Y. Y. Li, J. Lu and B. Huang, *ACS Appl. Mater. Interfaces*, 2018, **10**, 36157.
46 T. Yamase and H. Naruke, *J. Phys. Chem. B*, 1999, **103**, 8850.
47 M. Shang, C. Li and J. Lin, *Chem. Soc. Rev.*, 2014, **43**, 1372.
48 Y. Cheng, Y. Gao, H. Lin, F. Huang and Y. Wang, *J. Mater. Chem. C*, 2018, **6**, 7462.
49 Y. Liu, G. X. Liu, J. X. Wang, X. T. Dong and W. S. Yu, *Inorg. Chem.*, 2014, **53**, 11457.
50 R. Praveena, V. S. Sameera, P. Babu, C. Basavapoornima and C. K. Jayasankar, *Opt. Mater.*, 2017, **72**, 666.
51 H. Wu, B. Yan, H. Li, V. Singh, P. Ma, J. Niu and J. Wang, *Inorg. Chem.*, 2018, **57**, 7665.
52 X. Xu, H. Li, S. Xie, L. Mei, R. Meng, L. Chen and J. Zhao, *Inorg. Chem.*, 2020, **59**, 648.
53 X. Xu, R. Meng, C. Lu, L. Mei, L. Chen and J. Zhao, *Inorg. Chem.*, 2020, **59**, 3954.
54 M. Bösing, I. Loose, H. Pohlmann and B. Krebs, *Chem. – Eur. J.*, 1997, **3**, 1232.
55 J. Ying, Y.-G. Chen and X.-Y. Wang, *New J. Chem.*, 2019, **43**, 6765.
56 Y. Zhang, J. Jiang, Y. Liu, P. Li, Y. Liu, L. Chen and J. Zhao, *Nanoscale*, 2020, **12**, 10842.
57 J. Wang, W. Shi, S. Li, Q. Mao, P. Ma, J. Niu and J. Wang, *Dalton Trans.*, 2018, **47**, 7949.
58 J. W. Zhao, C. M. Wang, J. Zhang, S. T. Zheng and G. Y. Yang, *Chem. – Eur. J.*, 2008, **14**, 9223.
59 K. C. Szeto, K. P. Lillerud, M. Tilset, M. Bjørgen, C. Prestipino, A. Zecchina, C. Amberti and S. Bordiga, *J. Phys. Chem. B*, 2006, **110**, 21509.
60 S. Bordiga, A. Damin, F. Bonino, A. Zecchina, G. Spanò, F. Rivetti, V. Bolis, C. Prestipino and C. Lamberti, *J. Phys. Chem. B*, 2002, **106**, 9892.
61 H. Wu, M. Zhi, V. Singh, H. Li, P. Ma, J. Niu and J. Wang, *Dalton Trans.*, 2018, **47**, 13949.
62 M. Xia, X. Wu, Y. Zhong, H. T. Hintzen, Z. Zhou and J. Wang, *J. Mater. Chem. C*, 2019, **7**, 2927.
63 T. Ogi, Y. Kaihatsu, F. Iskandar, W.-N. Wang and K. Okuyama, *Adv. Mater.*, 2008, **20**, 3235.
64 W. Lü, Z. Hao, X. Zhang, Y. Luo, X. Wang and J. Zhang, *Inorg. Chem.*, 2011, **50**, 7846.
65 Y. M. Wu, Y. Cen, L. J. Huang, R. Q. Yu and X. Chu, *Chem. Commun.*, 2014, **50**, 4759.
66 H. Guan, Y. Sheng, Y. Song, C. Xu, X. Zhou, K. Zheng, Z. Shi and H. Zou, *J. Phys. Chem. C*, 2017, **121**, 23080.
67 (*a*) G. Galleani, S. H. Santagneli, Y. Ledemi and Y. Messaddeq, *J. Phys. Chem. C*, 2018, **122**, 2275; (*b*) S. He, H. Xia, Q. Tang, Q. Sheng, J. Zhang, Y. Zhu and B. Chen, *Cryst. Growth Des.*, 2017, **17**, 3163.
68 (*a*) Y. Zhang, W. T. Gong, J. J. Yu, H. C. Pang, Q. Song and G. L. Ning, *RSC Adv.*, 2015, **5**, 96272; (*b*) K. Panigrahi, S. Saha, S. Sain, R. Chatterjee, A. Das, U. K. Ghorai, N. Sankar Das and K. K. Chattopadhyay, *Dalton Trans.*, 2018, **47**, 12228.
69 I. Carrasco, F. Piccinelli, I. Romet, V. Nagirnyi and M. Bettinelli, *J. Phys. Chem. C*, 2018, **122**, 6858.
70 X. Zhou, H. Wang, S. Jiang, G. Xiang, X. Tang, X. Luo, L. Li and X. Zhou, *Inorg. Chem.*, 2019, **58**, 3780.
71 D. L. Dexter and J. A. Schulman, *J. Chem. Phys.*, 1954, **22**, 1063.
72 X. Zhang, L. Zhou, Q. Pang, J. Shi and M. Gong, *J. Phys. Chem. C*, 2014, **118**, 7591.
73 C.-H. Huang, P.-J. Wu, J.-F. Lee and T.-M. Chen, *J. Mater. Chem.*, 2011, **21**, 10489.
74 G. Blasse, *Phys. Lett. A*, 1968, **28**, 444.
75 G. Blasse, *J. Solid State Chem.*, 1986, **62**, 207.
76 F. Kang, L. Li, J. Han, D. Y. Lei and M. Peng, *J. Mater. Chem. C*, 2017, **5**, 390.
77 K. Li, S. S. Liang, M. M. Shang, H. Z. Lian and J. Lin, *Inorg. Chem.*, 2016, **55**, 7593.
78 Q. Wang, H. S. Xu, F. Z. Zhang and Z. H. Wang, *Optik*, 2017, **129**, 21.
79 A. Kapogiannatou, E. Paronis, K. Paschidis, A. Polissidis and N. G. Kostomitsopoulos, *Appl. Anim. Behav. Sci.*, 2016, **184**, 135.
80 Y. Zhang, W. Gong, J. Yu, H. Pang, Q. Song and G. Ning, *RSC Adv.*, 2015, **5**, 62527.
81 J. Suresh Kumar, K. Pavani, A. Mohan Babu, N. Kumar Giri and S. B. Rai, *J. Lumin.*, 2010, **130**, 1916.
82 C. S. McCamy, *Color Res. Appl.*, 1992, **17**, 142.